Temperature-renormalized phonon and electron transport in thermoelectric Mg_3Sb_2: Dominant role of anharmonic phonon modes

Jinzi Yu,[1,*] Ran Zhou,[1,2,*] Fang Lv,[1] Hanpu Liang,[3] Hongliang Shi,[2,†] and Yifeng Duan[1,‡]
[1]*School of Materials and Physics, China University of Mining and Technology, Xuzhou, Jiangsu 221116, China*
[2]*Department of Physics, Beihang University, Beijing 100191, China*
[3]*Beijing Computational Science Research Center, Beijing 100193, China*

(Received 17 October 2023; revised 21 December 2023; accepted 22 December 2023; published 18 January 2024)

Layered thermoelectric Mg_3Sb_2 has inspired increasing interest due to its inherently peculiar phonon and electron properties. Here, we propose the crucial role of temperature-induced renormalization of phonon and electron transports in the thermal, electronic, and thermoelectric performance by considering the peculiar temperature-dependent anharmonic phonon vibrational modes. After the phonon renormalization is included, the lattice thermal conductivity has a very weak temperature dependence of $\sim T^{-0.62}$ that agrees better with the experimental results than other theoretical pictures, in sharp contrast to the traditional harmonic T^{-1} trend. This is because the strong quartic anharmonicity induces significant hardening of low-lying acoustic phonon modes at the Brillouin zone boundary with temperature and finally suppresses the scattering rate by reducing the phonon scattering phase space. The fundamental band gap anomalously increases with temperature rather than decreasing as in most semiconductors because the greatly strengthened electron-acoustic-phonon coupling by locally asymmetric atomic vibrations drops the valence band maximum significantly. Furthermore, the temperature dependence of thermopower is effectively improved by the temperature-renormalized electronic structures, and then, combined with the phonon renormalization, excellent thermoelectric performance in good agreement with the experimental data is described. Our work establishes the relationship of temperature-renormalized phonon and electron transports versus intrinsic anharmonic acoustic phonon modes, which is helpful for describing the related physical properties more precisely at elevated temperatures.

DOI: 10.1103/PhysRevB.109.014311

I. INTRODUCTION

The layered compound Mg_3Sb_2 is a well-known *n*-type thermoelectric (TE) material near room temperature due to the low lattice thermal conductivity κ_L and excellent electron transport properties [1–3]. At present, accurately predicting the phonon properties of this strongly anharmonic material remains challenging; for example, the temperature dependence of κ_L is $\sim T^{-0.48}$ in theory but in the wide range from $\sim T^{-0.57}$ to $\sim T^{-0.9}$ in experiment [4–7]. In the conventional harmonic T^{-1} approximation, the temperature-dependent κ_L is solely decided by the phonon occupation number [8]. The temperature-induced phonon renormalization usually changes the relationships of phonon scattering phase space and group velocity versus temperature to further improve the temperature-dependent κ_L [9–12]. In Mg_3Sb_2 [4], the noticeable discrepancy between predicted and measured data is attributed to neglecting the four-phonon (4ph) scattering process, although the temperature-renormalized second- and third-order interatomic force constants (IFCs) have been included. Here, we systematically explore the anomalous phonon phenomenon by disclosing how the temperature-dependent 4ph scattering phase space and phonon population affect the scattering rate, highlighting the importance of phonon renormalization and 4ph scattering process in the thermal transport of strongly anharmonic materials.

Excellent thermopower is another key to the high TE performance of Mg_3Sb_2 because of the peculiar band structure with a sixfold-degenerate conduction band edge [13,14]. In general, accurately describing the band structures at different temperatures, i.e., the device operating conditions, is practically needed. Unfortunately, these temperature effects are usually ignored in the majority of theoretical TE studies since the first-principles calculations are largely performed for the $T = 0$ K ground state [15,16]. Temperature, as one of the most fundamental thermodynamic parameters, governs the electronic structure and related physical properties, i.e., the band gap, carrier effective mass and mobility, optical absorption, and so on. For instance, the carrier effective mass strongly depends on the temperature-renormalized electronic structure [17,18], which significantly affects the Seebeck coefficient S, the electrical conductivity σ, and, eventually, the TE performance.

The dependence of electronic structure on temperature is ascribed to two main mechanisms. One is the lattice thermal expansion, as reported recently in TE materials, such as PbTe, $CoSb_3$, and SnTe [19–21]. The other is the lattice dynamics, such as the atomic vibration induced by the activated phonon mode, known as the electron-phonon renormalization (EPR)

*These authors contributed equally to this work.
†hlshi@buaa.edu.cn
‡yifeng@cumt.edu.cn

[22–26]. Taking PbTe as an example, the increasing off-center displacement of the Pb atom with temperature results in the convergence of energy bands [27]. Here, to describe the electron transport more accurately than the conventional treatments for practical applications of Mg_3Sb_2, we utilize the recently developed "one-shot" (also known as the "frozen-phonon") method to evaluate the temperature dependence of electronic structure and thus to establish the relationship of carrier effective mass versus temperature. The computational efficiency and accuracy of this method in predicting the effective electronic structures at different temperatures have been widely verified [28,29].

In this work, we focus on the temperature-renormalized phonon and electron transports in Mg_3Sb_2 by relating them to the peculiar low-lying acoustic phonon modes at the Brillouin zone boundary. On the one hand, the temperature-dependent κ_L is significantly weakened to quantitatively and qualitatively match better with the measured data than available theoretical results by including the anharmonic phonon renormalization and, particularly, the 4ph scattering process because of the typical quartic character of anharmonicity. The temperature-induced hardening of acoustic phonon modes noticeably reduces the 4ph scattering phase space to offset the temperature-enhanced phonon population to further weaken the dependence of phonon scattering rate on temperature. On the other hand, in contrast to Varshni's relation [30–32], the band gap unexpectedly increases with temperature, e.g., by at least 50% between 0 and 700 K, based on the one-shot configurations accounting for the effects from both lattice thermal expansion via the quasiharmonic approximation (QHA) and lattice vibrations via the frozen-phonon method. The locally asymmetric atomic vibrations of acoustic phonon modes greatly strengthen the electron-phonon coupling, inducing the anomalously fast drop of the valence band maximum with temperature. Finally, the temperature-dependent S and σ are improved by the phonon-renormalized carrier effective masses at different temperatures. Our work provides a comprehensive understanding of TE performance from the point of view of the temperature-induced renormalization of phonon and electron transports in Mg_3Sb_2.

II. COMPUTATIONAL METHODS

The temperature-dependent effective potential (TDEP) technique, a thorough and accurate method to determine the anharmonic free energy, is based on the *ab initio* molecular dynamics (AIMD), followed by a mapping onto a model Hamiltonian [33–35]. The effective Hamiltonian at each temperature is fitted by the TDEP method as

$$H = \overbrace{U_0 + \sum_i \frac{\mathbf{p}_i^2}{2m_i} + \frac{1}{2}\sum_{ij\alpha\beta}\Phi_{ij}^{\alpha\beta}u_i^\alpha u_j^\beta}^{H_0} + \underbrace{\frac{1}{3!}\sum_{ijk\alpha\beta\gamma}\Phi_{ijk}^{\alpha\beta\gamma}u_i^\alpha u_j^\beta u_k^\gamma}_{H_3} + \underbrace{\frac{1}{4!}\sum_{ijkl\alpha\beta\gamma\delta}\Phi_{ijkl}^{\alpha\beta\gamma\delta}u_i^\alpha u_j^\beta u_k^\gamma u_l^\delta}_{H_4}. \tag{1}$$

Here, U_0 is a constant energy; p_i and m_i are the momentum and mass of atom i, respectively; u_i^α is the displacement of atom i in the Cartesian direction α; and $\Phi_{ij}^{\alpha\beta}$, $\Phi_{ijk}^{\alpha\beta\gamma}$, and $\Phi_{ijkl}^{\alpha\beta\gamma\delta}$ are the elements of the second-, third-, and fourth-order IFCs, respectively. We fit IFCs of increasing order in a sequential fashion; that is, we first find the best possible fit of the AIMD forces using just the second-order IFCs, then fit the third-order IFCs to the residual atomic forces, and then similarly fit the fourth-order IFCs. This fitting scheme ensures that H_0 in Eq. (1) is the largest, while the effects of H_3 and H_4 can be treated as perturbations [8].

A set of renormalized phonon normal mode frequencies is obtained from H_0, where $\mathbf{q}$ is the wave vector and s is the branch index. The lowest-order contribution to the phonon self-energy contains the terms from both third- and fourth-order IFCs, i.e., $\sum_{\mathbf{q}s}(\Omega) = \sum_{\mathbf{q}s}^{(3)}(\Omega) + \sum_{\mathbf{q}s}^{(4)}$, where Ω is the frequency, $\sum_{\mathbf{q}s}^{(3)}(\Omega) = \Delta_{\mathbf{q}s}^{(3)}(\Omega) + i\Gamma_{\mathbf{q}s}^{(3)}(\Omega)$, and $\sum_{\mathbf{q}s}^{(4)} = \Delta_{\mathbf{q}s}^{(4)}$ [36]. $\Delta_{\mathbf{q}s}^{(3)}(\Omega)$, $\Gamma_{\mathbf{q}s}^{(3)}(\Omega)$, and $\Delta_{\mathbf{q}s}^{(4)}$ are temperature dependent, and the explicit form of this self-energy is described in Sec. I of the Supplemental Material [37] (see also references [36,38] therein). The phonon spectral function is obtained from the renormalized phonon frequency and self-energy as

$$S(\mathbf{q},\Omega) = \sum_s \frac{2\omega_{\mathbf{q}s}\Gamma_{\mathbf{q}s}(\Omega)}{\left(\Omega^2 - \omega_{\mathbf{q}s}^2 - 2\omega_{\mathbf{q}s}\Delta_{\mathbf{q}s}^{(3+4)}\right)^2 + 4\omega_{\mathbf{q}s}^2\Gamma_{\mathbf{q}s}^{(3)}(\Omega)^2}. \tag{2}$$

The energy change $\Delta E_{n\mathbf{k}}(T)$ of the electronic state at band n, wave vector $\mathbf{k}$, and temperature T is described by [28,29]

$$\Delta E_{n\mathbf{k}}(T) = \Delta E_{n\mathbf{k}}^{\mathrm{LE}}(T) + \Delta E_{n\mathbf{k}}^{\mathrm{VIB}}(0) + \Delta E_{n\mathbf{k}}^{\mathrm{VIB}}(T). \tag{3}$$

The first term describes the lattice thermal expansion. The second term, referred to as the zero-point renormalization (ZPR), represents the energy change from the zero-point vibrations at $T = 0$ K. $\Delta E_{n\mathbf{k}}^{\mathrm{VIB}}(T)$ represents the energy shift and the lifetime broadening caused by temperature through the EPR for all phonon modes of branch j, wave vector $\mathbf{q}$, and frequency $\omega_{j\mathbf{q}}$ [39],

$$\Delta E_{n\mathbf{k}}^{\mathrm{VIB}}(T) = \sum_{j\mathbf{q}} \frac{\partial E_{n\mathbf{k}}}{\partial n_{j\mathbf{q}}}\left(n_{j\mathbf{q}}(T) + \frac{1}{2}\right), \tag{4}$$

where $n_{j\mathbf{q}} = (e^{\beta\hbar\omega_{j\mathbf{q}}} - 1)^{-1}$ is the Bose-Einstein phonon occupation factor with $\beta = 1/k_BT$. The real part of the complex interaction coefficient $\partial E_{n\mathbf{k}}/\partial n_{j\mathbf{q}}$ contributes to the energy shift of the bands and contains both Debye-Waller (DW) and self-energy (SE) parts, whereas the imaginary part leads to a lifetime broadening of the electronic states. Obviously, the band gap renormalization is determined by the difference in magnitude and the sign of the respective energy shift of the valence and conduction bands.

Invoking energy conservation transforms the summation in Eq. (4) into an integral over the phonon frequencies [39]:

$$\Delta E_{n\mathbf{k}}^{\mathrm{VIB}}(T) = \int_0^\infty d\omega g^2F(n,\mathbf{k},\omega)\cdot\left(n_{j\mathbf{q}}(T) + \frac{1}{2}\right),$$
$$g^2F(n,\mathbf{k},\omega) = \sum_{j\mathbf{q}}\frac{\partial E_{n\mathbf{k}}}{\partial n_{j\mathbf{q}}}\delta(\omega - \omega_{j\mathbf{q}}). \tag{5}$$

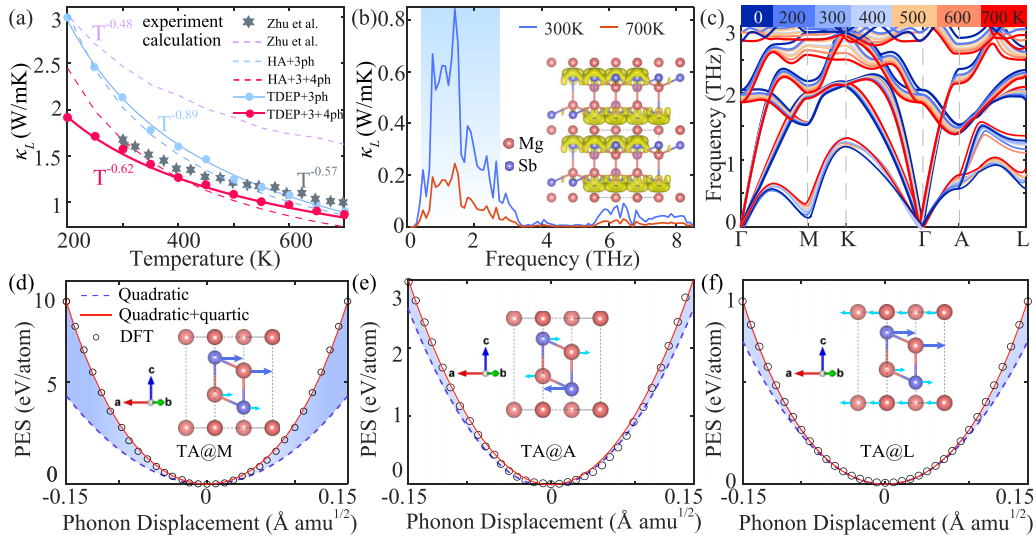

FIG. 1. (a) Temperature-dependent κ_L in Mg_3Sb_2 at different theoretical levels, together with the experimental data for comparison [4]. (b) Frequency-dependent κ_L at 300 and 700 K. (c) Temperature-dependent phonon in the temperature range from 0 to 700 K. (d)–(f) Potential energy surfaces (PESs) of the low-lying transverse acoustic phonon mode at the Brillouin zone boundary M, A, and L points, respectively, together with the corresponding phonon vibrational modes in the insets.

The electron-phonon spectral function $g^2F(n,\mathbf{k},\omega)$ is essentially the phonon density of states (DOS) appropriately weighted by the electron-phonon matrix elements. As such, the spectral function is temperature independent, which means that the temperature dependence of the electron-phonon contribution to the gap shift arises solely from the Bose-Einstein occupation factor $n_{j\mathbf{q}}(T)$. The one-shot method allows efficient evaluation of these thermal effects, together with the theory and computational details described in Sec. II of Supplemental Material [37] (see also references [28,29,40–42] therein).

The density functional theory (DFT) calculations were performed within the Perdew-Burke-Ernzerhof (PBE) generalized gradient approximation as implemented in the VASP package [43–47]. A 500 eV plane-wave energy cutoff and the Γ-centered **K** meshes with $2\pi \times 0.05$ Å^{-1} resolution for Brillouin zone sampling were adopted to ensure convergence within 10^{-8} eV and 10^{-5} eV/Å for energy and force, respectively. The phonon dispersion, the second-order IFCs, and the QHA method [40] were calculated by the PHONOPY package [48]. The temperature-dependent phonon frequencies including anharmonic effects were evaluated by the DYNAPHOPY code to process the VASP AIMD trajectories [49]. The AIMD simulations based on the lattice parameters at T calculated by the QHA method were performed in the NVT ensemble using a Nosé-Hoover thermostat with the default Nosé mass as set by VASP and two femtosecon time steps. The third-order IFCs, controlling the three-phonon (3ph) scattering rates, were obtained with the THIRDORDER package [50]. The fourth-order IFCs, controlling the 4ph scattering rates, were calculated using the FOURPHONON package [51]. The effective band structure (EBS) was obtained by unfolding the band structure of the supercell using the BANDUP code to transform the eigenstates from the supercell into a primitive cell [52,53]. The phonon transport properties were evaluated using the Boltzmann transport equation $\kappa_L = \Sigma_\lambda C_\lambda v_\lambda^2 \tau_\lambda$ as implemented in the SHENGBTE code [50]. The electrical conductivity σ and Seebeck coefficient S were calculated with the AMSET package by including the effects of acoustic deformation potential scattering, polar optical phonon scattering, and ionized impurity scattering [54,55]. More computational details are described in Sec. III of the Supplemental Material [37], and the convergence tests are shown in Figs. S1 and S2 [37].

III. RESULTS AND DISCUSSION

Pristine Mg_3Sb_2 is composed of the ionic Mg^{2+} layer (the Mg atoms labeled as Mg1) and the covalent $[Mg_2Sb_2]^{2-}$ layer (the Mg atoms labeled as Mg2) in the stable Zintl-type structure with the $P\bar{3}m1$ space group, where the Mg1 atom is on the octahedron site and the Mg2 atom is on the tetrahedron site. The partitioning of the Mg site reflects the very significant difference in the local bonding environment (e.g., the chemical bond strength), which induces the strong anharmonic effect, reducing κ_L. We explore the effects of temperature-induced anharmonic phonon renormalization and 4ph scattering on κ_L of Mg_3Sb_2. There are two main features in the temperature-dependent κ_L calculations. One is the thermal expansion effects; the other is the anharmonic renormalization of the second-order IFCs extracted from the AIMD under the corresponding volumes at finite temperatures.

Figure 1(a) displays the temperature-dependent κ_L at different theoretical levels together with the available experimental data for comparison [4]. After including the 3ph scattering process and the temperature-dependent second-order IFCs in the TDEP+3ph model, the temperature dependence of κ_L is weakened as the $\sim T^{-0.89}$ relation, which seriously deviates from the experimental data, especially at relatively low temperatures. After further including the renormalized third-order IFCs in the TDEP+3ph model [4], the

temperature dependence of κ_L is improved to $\sim T^{-0.48}$ in the trend, compared to the experimental $\sim T^{-0.57}$; however, κ_L is much larger than the experimental data in magnitude because higher-order anharmonicity and phonon scattering are ignored. When the renormalized second-order IFCs and the three- and four-phonon (3+4ph) scattering rates are included in the TDEP + 3 + 4ph model, $\kappa_L \sim T^{-0.62}$ matches the experimental data much better than any other theoretical results not only in the trend but also in magnitude. This highlights the importance of high-order anharmonicity in determining thermal transport in strongly anharmonic crystals, particularly at elevated temperatures.

The serious deviation of κ_L from the traditional T^{-1} trend reveals the complex role of high-order anharmonic effects in that they not only lead to the additional phonon scattering rates but also induce the phonon mode shifts at finite temperatures; therefore, the corresponding change in κ_L is usually nontrivial. The frequency-dependent κ_L at 300 and 700 K, as displayed in Fig. 1(b), reveals that κ_L mainly arises from the low-frequency acoustic phonon modes below 2.5 THz. Figure 1(c) shows the temperature-dependent phonon dispersions at different temperatures in the corresponding low-frequency range. It is interesting to note that the phonon modes share the distinct temperature dependence. Specifically, as temperature increases, the low-lying transverse acoustic phonon mode unexpectedly becomes hard, especially at the Brillouin zone boundary M, A, and L points, while the other phonon modes routinely become soft; therefore, the scattering phase space is greatly reduced to suppress the phonon scattering. This phenomenon is unusual, as most materials usually show phonon softening due to weakened bond strengths with increasing temperature, which is confirmed by the positive Grüneisen parameters in Fig. S3 [37].

To provide an intuitive physical picture of the anomalous phonon hardening, we visualize the intrinsic low-lying transverse acoustic phonon modes at the M, A, and L points in the insets of Figs. 1(d)–1(f). These phonon modes mainly characterize the in-plane asymmetric atomic vibrations within the $[Mg_2Sb_2]^{2-}$ layer, which is driven by the peculiar weak ionic bonding between the Mg^{2+} and strongly covalent bonding $[Mg_2Sb_2]^{2-}$ layers in the hierarchical bond structure, as shown in the inset of Fig. 1(b). In detail, atoms within the $[Mg_3Sb_2]^{2-}$ layer vibrate along the same direction but with different amplitudes at the M point but along opposite directions at the A point. In contrast, at the L point, the in-plane vibrations of the Mg^{2+} and $[Mg_3Sb_2]^{2-}$ layers have opposite directions. Therefore, the phonon vibrational mode at the M point has the most remarkable asymmetric character and dominates the anharmonicity, which is confirmed by the lowest phonon frequency, as illustrated in Fig. 1(c).

To further quantify the anharmonicity, we calculate the potential energy surfaces (PESs) with respect to the phonon displacement of the low-lying transverse acoustic phonon modes at the Brillouin zone boundary M, A, and L points in Figs. 1(d)–1(f). All the PESs show the presence of a relatively deep energy well with a flat bottom and deviate remarkably from the harmonic (i.e., second-order fitting) term when atomic collective motions have a large magnitude at elevated temperature. The more significant the deviation from the quadratic function is, the stronger the anharmonicity is. The energy variation is approximated by a fourth-order polynomial as $\Delta E(\Delta r) = k_2(r - r_0)^2 + k_4(r - r_0)^4$, where the third-order coefficient $k_3 = 0$; therefore, the cubic anharmonicity is negligible, and the quartic anharmonicity is dominant in the thermal transport, especially at high temperatures. This clearly explains the fact that introducing only the renormalized third-order IFCs into the TDEP+3ph model cannot effectively improve the temperature-dependent κ_L, which is much larger than the experimental data, as reported in Ref. [4]. Furthermore, at the M point, $k_4 = 3467.4$ eV/Å^4, which is at least one order of magnitude larger than 149.3 and 239.1 eV/Å^4 at the A and L points, respectively. The quartic anharmonicity mainly stems from the locally asymmetric atomic vibrations at the M point within the $[Mg_2Sb_2]^{2-}$ layer. As temperature increases, this anharmonicity is strengthened to harden the low-lying transverse acoustic phonon modes. As a comparison, the lowest optical phonon mode at the Γ point displays the typical harmonic character confirmed by the perfect second-order fitting of the PES in Fig. S4 [37]. This phonon mode is noticeably softened by increasing temperature because of the thermal expansion effects in that the bond strength is weakened to suppress the harmonic atomic vibration.

Renormalized phonon dispersions can affect the phonon group velocity, phonon scattering phase space, and, consequently, κ_L. When the anharmonic phonon is renormalized by increasing temperature, the shapes (i.e., the slopes) of the phonon branches are nearly unchanged, indicating the negligible variation of group velocity, as shown in Figs. 1(c) and S5 [37]. The weighted phase space (WPS) that quantifies the symmetry-allowed phonon scattering channels is expressed as

$$\mathrm{WPS} = \frac{\Omega}{(6\pi n)^3} \sum_{p,p_1,p_2} \iint \delta[\omega_p(q) + \omega_{p_1}(q_1) - \omega_{p_2}(q + q_1 - Q)] d^3q_1 d^3q, \tag{6}$$

where the phonon frequency meets the conservation of momentum and energy [56]. Here, the anharmonic phonon renormalization results in the noticeable hardening of low-frequency phonon modes to reduce the phonon scattering channels due to the prohibition of energy and momentum conservation laws. More importantly, as temperature increases, the 4ph scattering WPS is significantly reduced, while the 3ph WPS remains nearly unaffected, which is totally different from the routine inversely proportional relationship of the 3ph and 4ph scatterings versus temperature in the harmonic approximation, as shown in Figs. 2(a) and S6 [37]. Note that, compared to the phonon-phonon scattering, the isotope scattering is not at all dominant in the thermal transport, as shown in Fig. S7 [37]. This unexpected phenomenon is ascribed to the dominant quartic anharmonicity induced by the peculiar asymmetric vibrational modes at the Brillouin zone boundary. On the other hand, the scattering rates are

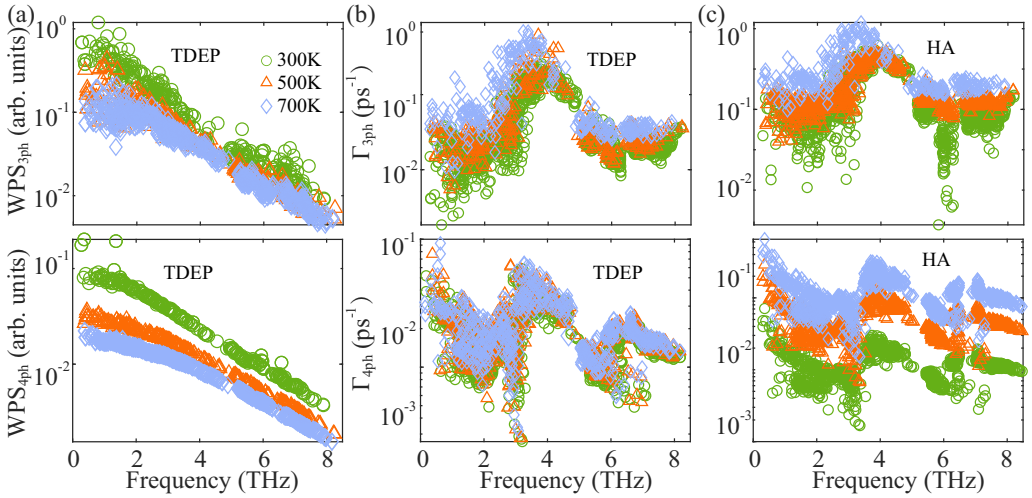

FIG. 2. (a) Weighted phase spaces WPS_{3ph} and WPS_{4ph} in Mg_3Sb_2 with the anharmonic phonon renormalization. Phonon scattering rates Γ_{3ph} and Γ_{4ph} (b) with and (c) without the anharmonic phonon renormalization.

expressed as

$$\Gamma^{(\pm)}_{\lambda\lambda'\lambda''} = \frac{\hbar\pi}{4}\frac{\begin{Bmatrix} n_{\lambda'} - n_{\lambda''} \\ n_{\lambda'} - n_{\lambda''} + 1 \end{Bmatrix}}{\omega_\lambda\omega_{\lambda'}\omega_{\lambda''}}|V^{(\pm)}_{\lambda\lambda'\lambda''}|^2\delta(\omega_\lambda \pm \omega_{\lambda'} - \omega_{\lambda''}) \tag{7}$$

$$\Gamma^{\substack{++\\(+-)\\--}}_{\lambda\lambda'\lambda''\lambda'''} = \frac{\hbar^2\pi}{8N}\frac{\begin{Bmatrix} (1+n_{\lambda'})(1+n_{\lambda''})n_{\lambda'''} \\ (1+n_{\lambda'})n_{\lambda''}n_{\lambda'''} \\ n_{\lambda'}n_{\lambda''}n_{\lambda'''} \end{Bmatrix}}{n_\lambda} \times |V^{\substack{++\\(+-)\\--}}_{\lambda\lambda'\lambda''\lambda'''}|^2\frac{\delta\left(\omega_\lambda\begin{bmatrix}+\\+\\-\end{bmatrix}\omega_{\lambda'}\begin{bmatrix}+\\-\\-\end{bmatrix}\omega_{\lambda''} - \omega_{\lambda'''}\right)}{\omega_\lambda\omega_{\lambda'}\omega_{\lambda''}\omega_{\lambda'''}}, \tag{8}$$

where Eqs. (7) and (8) are the 3ph and 4ph scattering processes, respectively [51]. According to the Bose-Einstein distribution, the phonon occupation number n_λ of the λ mode is proportional to temperature at the high-temperature limit; therefore, increasing temperature enhances the phonon scattering rates Γ_{3ph} and Γ_{4ph} proportionally. Since the 3ph WPS is insensitive to temperature, the temperature-dependent n_λ is dominant in the thermal transport, and thus, the TDEP and harmonic pictures have very similar relationships of Γ_{3ph} versus temperature, favoring the $\kappa_L \sim T^{-1}$ trend. When the TDEP + 3 + 4ph mode is included to consider the strong quartic anharmonicity, the completely opposite dependence of the 4ph WPS and n_λ on temperature makes Γ_{4ph} comparable overall at different temperatures, in contrast to the conventional $\propto T$ relationship in the harmonic picture, as illustrated in Figs. 2(b) and 2(c). As a result, in comparison with the traditional $\sim T^{-1}$ trend, the temperature dependence of κ_L is greatly weakened to $\sim T^{-0.62}$, agreeing well with the experimental $\sim T^{-0.57}$ [4]. Moreover, Fig. S8 [37] shows that the umklapp process contributes more to the 4ph process scattering overall than the normal process.

Mg_3Sb_2 is an indirect band gap semiconductor with orbital-projected valence and conduction bands near the Fermi level in Fig. 3(a). The valence band states have the typical bonding character and are from the Sb *p* orbitals. Especially, the valence band maximum (VBM) at the Γ point is dominated by the Sb p_z orbital due to the symmetry-allowed splitting effects. The conduction band states have the antibonding character and are mainly from the Mg *s* orbital. The EBSs by unfolding the supercell band structures are calculated at the PBE functional level. Despite the underestimated band gap, other qualitative characteristics of the band structure are reproduced in comparison with the Heyd-Scuseria-Ernzerhof functional [57,58], where the computations are very expensive because of the large one-shot supercells. In the one-shot picture, only a single effective lattice structure, obtained by displacing atoms from the equilibriums via summation over

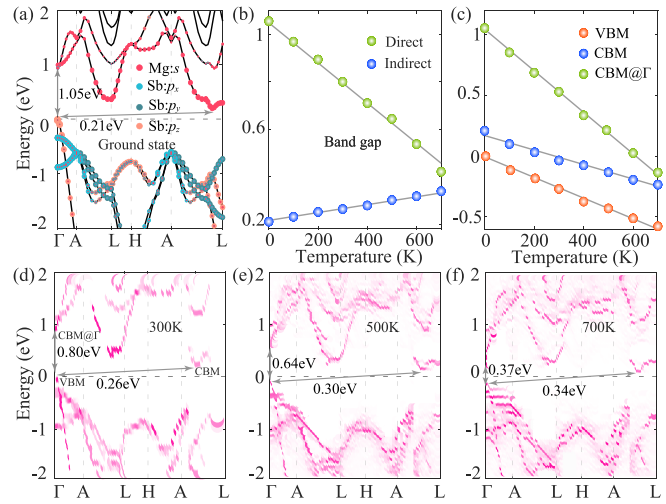

FIG. 3. (a) Orbital-projected band structure of ground-state Mg_3Sb_2. (b) Indirect and direct electronic band gaps as a function of temperature. (c) Energy levels of the VBM, CBM, and CBM@Γ states as a function of temperature with respect to the Sb 1*s* orbital level as the reference; the VBM level at 0 K is set to zero. (d)–(f) Effective band structures with EPR effects at 300, 500, and 700 K, respectively.

the Bose-Einstein-weighted phonon vibration eigenmodes, is used to represent the effects of thermal vibrations at each temperature [59]. To confirm the reliability of the one-shot picture, Fig. S9 [37] displays the relationship of the band gap with AIMD time at different temperatures, which agrees well with the one-shot results.

Figure 3(b) shows the anomalous temperature-dependent band gaps from the EBSs. As temperature increases, the indirect band gap unexpectedly increases by at least 50% in the temperature range from 0 to 700 K with the conduction band minimum (CBM) near the L point, contrary to the case in most semiconductors. In sharp contrast, the energy gap between the bottom conduction band at the Γ point (called the CBM@Γ hereafter) and the VBM obeys the routine Varshni relation $E_g = E_0\text{-}aT^2/(T+b)$ and decreases with temperature, where $a = 1.617 \times 10^{-3}$ eV/K and $b = -26.54$ K. Figure 3(c) shows that, as temperature increases, the VBM, CBM, and CBM@Γ simultaneously linearly decrease with respect to the deepest Sb 1s orbital level, but the CBM drops slower, and the CBM@Γ drops faster than the VBM, which eventually results in the anomalous dependence of the band gap on temperature. As depicted in Eq. (3), the energy change in the electronic structure is determined by the lattice thermal expansion, ZPR, and EPR. Figure S10 [37] reveals that the ZPR contribution is negligible by showing almost the same EBSs with and without the ZPR effects. Figure S11 [37] shows that when the lattice thermal expansion alone is included, the indirect band gap indeed linearly decreases with temperature, as is common in most semiconductors. Therefore, the anomalous increase in band gap with temperature is ascribed to the EPR effects.

To describe how the EPR effect evolves with temperature in detail, Figs. 3(d)–3(f) show the typical EBSs at 300, 500, and 700 K, respectively, together with the corresponding one-shot configurations in Fig. S12 [37]. As the thermally induced atomic distortion breaks the symmetry of the ground-state configuration, the unfolded electronic structure exhibits smeared and blurred bands with a reduced spectral weight, reflecting the perturbed Bloch characteristic [60]. According to the empirical pseudopotential method [39,61], both DW and SE terms cause the moderate energy downshift of the conduction band with increasing temperature, as confirmed by Fig. 3(c). The orbital hybridization between the Mg s and Sb p states at the Γ point results in a faster drop of the CBM@Γ than the CBM. For the valence band states, the DW correction is positive, and the SE correction depends on the particular phonon modes involved in the EPR interaction. In conventional semiconductors, the acoustic phonon SE contribution is generally negative, canceling out the DW contribution; therefore, only the positive optical phonon SE term pushes the VBM level up to reduce the band gap. However, in Mg_3Sb_2, the acoustic phonon couples more strongly with the electron than the optical phonon because of the peculiar temperature-induced acoustic phonon hardening, especially at the Brillouin zone boundary. As sketched in Fig. S13 [37], the enlarged acoustic phonon SE term overwhelms the DW term to drive the remarkable downshift of VBM with temperature for the anomalous increase in band gap due to the temperature-strengthened electron-acoustic-phonon coupling.

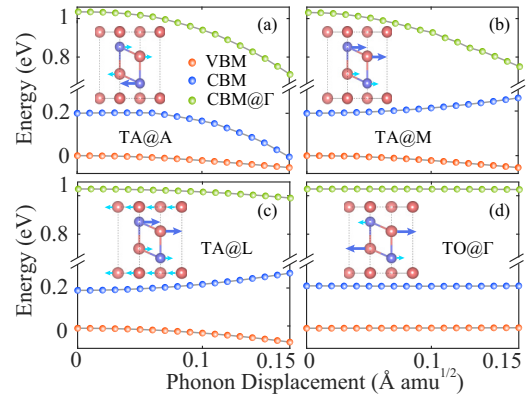

FIG. 4. Energy levels of the VBM, CBM, and CBM@Γ states as a function of phonon mode amplitude: (a)–(c) the TA mode at the A, M, and L points, respectively, and (d) the lowest TO mode at the Γ point. The deepest Sb 1s orbital level is used as the reference, and the VBM of the zero phonon amplitude at $T = 0$ K is set to zero.

To verify the dominant role of EPR in the anomalous temperature dependence of the band gap, we focus on the effects of anharmonic acoustic phonon TA modes at the M, A, and L points and the lowest harmonic optical phonon TO mode at the Γ point on the energy levels at the VBM, CBM, and CBM@Γ as a function of the corresponding phonon mode amplitudes in the primitive cell, as shown in Fig. 4. Here, the Sb 1s level is set as the reference because of the lowest orbital energy. The VBM decreases with increasing phonon amplitudes for the TA modes at the M, A, and L points. Meanwhile, although the TA mode at the A point decreases the CBM, the CBM is greatly enhanced by the TA modes at the M and L points, inducing the anomalous increase in the indirect band gap with temperature. Moreover, the TA modes drive the CBM@Γ to decrease faster than the VBM with increasing phonon amplitudes overall, especially for the phonon modes at the A and M points; therefore, the band gap at the Γ point decreases with temperature as in most semiconductors, consistent with the empirical pseudopotential model. In comparison, we also check the effect of a randomly selected harmonic phonon mode, i.e., the lowest TO mode at the Γ point, on the VBM, CBM, and CBM@Γ levels, which remain nearly unchanged as the harmonic phonon vibrational amplitudes increase. Therefore, the anomalous dependence of the band gap on temperature is attributed to the temperature-strengthened EPR by hardening the anharmonic acoustic phonon modes.

We next focus on the effects of the improved phonon and electron transports with the temperature-induced renormalizations on the TE performance characterized by the figure of merit $ZT = S^2\sigma T/(\kappa_e + \kappa_L)$, where the temperature-dependent carrier effective mass m^*, S, σ, and ZT for the p- and n-type dopings are illustrated in Fig. 5. The electron and hole m^*, calculated from the EBSs, significantly increase with temperature, as shown in Fig. 5(a). This is completely consistent with the transition from diffusive to localized electronic states near the Fermi level in disordered semiconductors at finite temperatures; that is, the enhanced disorder degree with increasing temperature makes the electronic states more localized, enhancing m^*. In the treatment of the Boltzmann

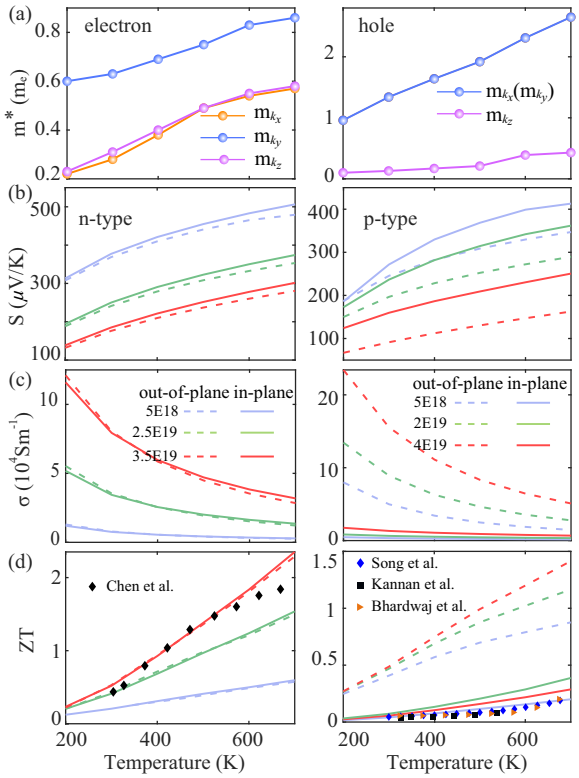

FIG. 5. Temperature-dependent (a) carrier effective mass m^*, (b) Seebeck coefficient S, (c) electrical conductivity σ, and (d) figure of merit ZT for the n- and p-type doping, together with the available experimental data for comparison.

transport equation, we substitute the conventional ground-state m^* from the band structure at $T = 0$ K of the primitive cell with the temperature-dependent m^* to improve the temperature dependence of $S = (2{k_B}^2/3e\hbar^2)m_d{}^*(\pi/3n)^{2/3}T$ and $\sigma = ne\mu_{2D}$ for better agreement of ZT with the experimental data than the traditional treatments [5,62–64], as shown in Figs. 5(b)–5(d). $m_d^* = N_v^{2/3}m_s^*$ is the DOS effective mass, N_v represents the valley degeneracy, m_s^* is the single-valley effective mass, and $\mu_{2D} = e\hbar^3 C_{2D}/(k_B T m^* m_d {E_d}^2)$. It is noteworthy that the optimal ZT is as high as 2.31 at 700 K with n-type doping concentration $\sim 3.5 \times 10^{19}$ cm^{-3}, which implies the great potential for practical applications in the TE field.

IV. CONCLUSIONS

In summary, we focused on the temperature dependence of thermal transport, electronic structure, and thermoelectric performance by including the temperature-dependent anharmonic renormalization of phonon and electron energies arising from an unusually strong quartic anharmonicity in Mg_3Sb_2. On the one hand, we showed the anomalous relationship of the lattice thermal conductivity versus temperature matches the experimental results better than in other theoretical pictures by unveiling the anharmonic acoustic phonon mode hardening. On the other hand, we revealed an anomalous increase in the band gap with temperature from the point of view of the temperature-strengthened electron-acoustic-phonon coupling instead of the lattice thermal expansion, which actually favors a decrease in the band gap. Finally, in comparison with conventional treatments of the Boltzmann transport equation, we improved the temperature dependence of the Seebeck coefficient and electrical conductivity to better describe the thermoelectric performance by including the temperature-dependent carrier effective masses, which are calculated from the effective band structures of the one-shot configurations. We expect that such temperature-induced effects are also crucial in other strongly anharmonic semiconductors, highlighting the growing need to account for temperature in the theoretical characterizations of thermal, electronic, and thermoelectric properties.

ACKNOWLEDGMENTS

The work is sponsored by the National Natural Science Foundation of China (Grants No. 12374079, No. 12174017, and No. 11774416) and the Assistance Program for Future Outstanding Talents of China University of Mining and Technology (Grant No. 2023WLJCRCZL274).

[1] F. Zhang, C. Chen, H. Yao, F. Bai, L. Yin, X. Li, S. Li, W. Xue, Y. Wang, F. Cao, X. Liu, J. Sui, and Q. Zhang, Adv. Funct. Mater. **30**, 1906143 (2020).
[2] X. Sun, X. Li, J. Yang, J. Xi, R. Nelson, C. Ertural, R. Dronskowski, W. Liu, G. J. Snyder, D. J. Singh, and W. Zhang, J. Comput. Chem. **40**, 1693 (2019).
[3] J. Zhang, L. Song, M. Sist, K. Tolborg, and B. B. Iversen, Nat. Commun. **9**, 4716 (2018).
[4] Y. Zhu, Y. Xia, Y. Wang, Y. Sheng, J. Yang, C. Fu, A. Li, T. Zhu, J. Luo, C. Wolverton, G. J. Snyder, J. Liu, and W. Zhang, Research **2020**, 4589786 (2020).
[5] L. Song, J. Zhang, and B. B. Iversen, J. Mater. Chem. A **5**, 4932 (2017).
[6] J. Shuai, Y. Wang, H. S. Kim, Z. Liu, J. Sun, S. Chen, J. Sui, and Z. Ren, Acta Mater. **93**, 187 (2015).
[7] A. Bhardwaj and D. K. Misra, RSC Adv. **4**, 34552 (2014).
[8] J. Klarbring, O. Hellman, I. A. Abrikosov, and S. I. Simak, Phys. Rev. Lett. **125**, 045701 (2020).
[9] R. Zhou, H. Liang, and Y. Duan, Appl. Phys. Lett. **122**, 082203 (2023).
[10] J. Yu, R. Zhou, H. Shi, and Y. Duan, J. Phys. Chem. Lett. **14**, 7975 (2023).
[11] Y. Zhao, C. Lian, S. Zeng, Z. Dai, S. Meng, and J. Ni, Phys. Rev. B **101**, 184303 (2020).
[12] Y. Zhao, S. Zeng, G. Li, C. Lian, Z. Dai, S. Meng, and J. Ni, Phys. Rev. B **104**, 224304 (2021).
[13] F. Meng, S. Sun, J. Ma, C. Chronister, J. He, and W. Li, Mater. Today. Phys. **13**, 100217 (2020).
[14] J. Zhang, L. Song, and B. B. Iversen, npj Comput. Mater. **5**, 76 (2019).
[15] J. Tani, M. Takahashi, and H. Kido, Phys. B (Amsterdam, Neth.) **405**, 4219 (2010).

[16] M. B. Maccioni, R. Farris, and V. Fiorentini, Phys. Rev. B **98**, 220301(R) (2018).
[17] F. Lv, H. Liang, and Y. Duan, Phys. Rev. B **107**, 045422 (2023).
[18] C. Lee, N. D. Rock, A. Islam, M. A. Scarpulla, and E. Ertekin, APL Mater. **11**, 011106 (2023).
[19] W. G. Zeier, A. Zevalkink, Z. M. Gibbs, G. Hautier, M. G. Kanatzidis, and G. J. Snyder, Angew. Chem., Int. Ed. **55**, 6826 (2016).
[20] R. Hanus, X. Guo, Y. Tang, G. Li, G. J. Snyder, and W. G. Zeier, Chem. Mater. **29**, 1156 (2017).
[21] J. D. Querales-Flores, P. Aguado-Puente, D. Dangić, J. Cao, P. Chudzinski, T. N. Todorov, M. Grüning, S. Fahy, and I. Savić, Phys. Rev. B **101**, 235206 (2020).
[22] S. Poncé, Y. Gillet, J. Laflamme Janssen, A. Marini, M. Verstraete, and X. Gonze, J. Chem. Phys **143**, 102813 (2015).
[23] S. Poncé, G. Antonius, Y. Gillet, P. Boulanger, J. Laflamme Janssen, A. Marini, M. Côté, and X. Gonze, Phys. Rev. B **90**, 214304 (2014).
[24] F. Giustino, Rev. Mod. Phys. **89**, 015003 (2017).
[25] F. Giustino, S. G. Louie, and M. L. Cohen, Phys. Rev. Lett. **105**, 265501 (2010).
[26] Y. Zhao, C. Lian, S. Zeng, Z. Dai, S. Meng, and J. Ni, Phys. Rev. B **102**, 094314 (2020).
[27] E. S. Božin, C. D. Malliakas, P. Souvatzis, T. Proffen, N. A. Spaldin, M. G. Kanatzidis, and S. J. L. Billinge, Science **330**, 1660 (2010).
[28] M. Zacharias, C. E. Patrick, and F. Giustino, Phys. Rev. Lett. **115**, 177401 (2015).
[29] M. Zacharias and F. Giustino, Phys. Rev. B **94**, 075125 (2016).
[30] T. Onuma, S. Saito, K. Sasaki, K. Goto, T. Masui, T. Yamaguchi, T. Honda, A. Kuramata, and M. Higashiwaki, Appl. Phys. Lett. **108**, 101904 (2016).
[31] Y. Varshni, Physica (Amsterdam) **34**, 149 (1967).
[32] A. Mock, J. VanDerslice, R. Korlacki, J. A. Woollam, and M. Schubert, Appl. Phys. Lett. **112**, 041905 (2018).
[33] O. Hellman, I. A. Abrikosov, and S. I. Simak, Phys. Rev. B **84**, 180301(R) (2011).
[34] O. Hellman, P. Steneteg, I. A. Abrikosov, and S. I. Simak, Phys. Rev. B **87**, 104111 (2013).
[35] O. Hellman and I. A. Abrikosov, Phys. Rev. B **88**, 144301 (2013).
[36] R. A. Cowley, Rep. Prog. Phys. **31**, 123 (1968).
[37] See Supplemental Material at http://link.aps.org/supplemental/10.1103/PhysRevB.109.014311 for more details on the phonon self-energy and one-shot theories, computational details, convergence tests, G parameters, the potential energy surface of the lowest-lying optical phonon mode at the Γ point, group velocity, weight phase spaces, isotope scattering, normal and umklapp processes, AIMD time-dependent band gaps at different temperatures, one-shot configurations with ZPR and EPR, lattice thermal expansion, and a sketch of the sign and magnitude of the DW and SE contributions.
[38] A. A. Maradudin, A. E. Fein, and G. H. Vineyard, Phys. Status Solidi B **2**, 1479 (1962).
[39] S. Gopalan, P. Lautenschlager, and M. Cardona, Phys. Rev. B **35**, 5577 (1987).
[40] A. Togo, L. Chaput, I. Tanaka, and G. Hug, Phys. Rev. B **81**, 174301 (2010).
[41] Y. Zhang, Z. Wang, J. Xi, and J. Yang, J. Phys.: Condens. Matter **32**, 475503 (2020).
[42] J. Ning, L. Zheng, W. Lei, S. Wang, J. Xi, and J. Yang, Phys. Chem. Chem. Phys. **24**, 16003 (2022).
[43] L. A. Burns, A. V. Mayagoitia, B. G. Sumpter, and C. D. Sherrill, J. Chem. Phys. **134**, 084107 (2011).
[44] J. P. Perdew, K. Burke, and M. Ernzerhof, Phys. Rev. Lett. **77**, 3865 (1996).
[45] J. Hafner, J. Comput. Chem. **29**, 2044 (2008).
[46] G. Kresse and J. Furthmüller, Phys. Rev. B **54**, 11169 (1996).
[47] G. Kresse and J. Hafner, Phys. Rev. B **49**, 14251 (1994).
[48] Y. Wang, S. L. Shang, H. Fang, Z. K. Liu, and L. Q. Chen, npj Comput. Mater. **2**, 16006 (2016).
[49] A. Carreras, A. Togo, and I. Tanaka, Comput. Phys. Commun. **221**, 221 (2017).
[50] W. Li, J. Carrete, N. A. Katcho, and N. Mingo, Comput. Phys. Commun. **185**, 1747 (2014).
[51] Z. Han, X. Yang, W. Li, T. Feng, and X. Ruan, Comput. Phys. Commun. **270**, 108179 (2022).
[52] P. V. C. Medeiros, S. Stafström, and J. Björk, Phys. Rev. B **89**, 041407(R) (2014).
[53] P. V. C. Medeiros, S. S. Tsirkin, S. Stafström, and J. Björk, Phys. Rev. B **91**, 041116(R) (2015).
[54] A. Faghaninia, G. Yu, U. Aydemir, M. Wood, W. Chen, G.-M. Rignanese, G. J. Snyder, G. Hautier, and A. Jain, Phys. Chem. Chem. Phys. **19**, 6743 (2017).
[55] A. M. Ganose, J. Park, A. Faghaninia, R. Woods-Robinson, K. A. Persson, and A. Jain, Nat. Commun. **12**, 2222 (2021).
[56] T. Pandey, C. A. Polanco, L. Lindsay, and D. S. Parker, Phys. Rev. B **95**, 224306 (2017).
[57] J. E. Peralta, J. Heyd, G. E. Scuseria, and R. L. Martin, Phys. Rev. B **74**, 073101 (2006).
[58] Y. Duan, L. Qin, L. Shi, G. Tang, and H. Shi, Appl. Phys. Lett. **100**, 022104 (2012).
[59] Z. Wang, J. Xi, J. Ning, K. Guo, B. Duan, J. Luo, G. J. Snyder, J. Yang, and W. Zhang, Chem. Mater. **33**, 1046 (2021).
[60] J. M. Adamczyk, F. A. Bipasha, G. A. Rome, K. Ciesielski, E. Ertekin, and E. S. Toberer, J. Mater. Chem. A **10**, 16468 (2022).
[61] P. Lautenschlager, P. B. Allen, and M. Cardona, Phys. Rev. B **31**, 2163 (1985).
[62] X. Chen, H. Wu, J. Cui, Y. Xiao, Y. Zhang, J. He, Y. Chen, J. Cao, W. Cai, S. J. Pennycook, Z. Liu, L.-D. Zhao, and J. Sui, Nano Energy **52**, 246 (2018).
[63] A. Bhardwaj, N. S. Chauhan, and D. K. Misra, J. Mater. Chem. A **3**, 10777 (2015).
[64] V. P. Kannan, V. Lourdhusamy, I. Paulraj, C.-J. Liu, and S. Madanagurusamy, ACS Appl. Mater. Interfaces **15**, 47058 (2023).